Strain to Ground Motion Conversion of DAS Data for Earthquake Magnitude and Stress Drop Determination

5 Itzhak Lior[1], Anthony Sladen[1], Diego Mercerat[2], Jean-Paul Ampuero[1], Diane Rivet[1], Serge Sambolian[1]

[1]Université Côte d'Azur, CNRS, Observatoire de la Côte d'Azur, IRD, Géoazur, France
[2]CEREMA, équipe MouvGS, Sophia Antipolis, Valbonne, France.

10 *Correspondence to*: Itzhak Lior (itzhaklior22@email.com)

Abstract. The use of Distributed Acoustic Sensing (DAS) presents unique advantages for earthquake monitoring compared with standard seismic networks: spatially dense measurements adapted for harsh environments and designed for remote operation. However, the ability to determine earthquake source parameters using DAS is yet to be fully established. In particular,
15 resolving the magnitude and stress drop, is a fundamental objective for seismic monitoring and earthquake early warning. To apply existing methods for source parameter estimation to DAS signals, they must first be converted from strain to ground motions. This conversion can be achieved using the waves' apparent phase velocity, which varies for different seismic phases ranging from fast body-waves to slow surface- and scattered-waves. To facilitate this conversion
20 and improve its reliability, an algorithm for slowness determination is presented, based on the local slant-stack transform. This approach yields a unique slowness value at each time instance of a DAS time-series. The ability to convert strain-rate signals to ground accelerations is validated using simulated data and applied to several earthquakes recorded by dark fibers of three ocean-bottom telecommunication cables in the Mediterranean Sea. The conversion emphasizes fast body-waves
25 compared to slow scattered-waves and ambient noise, and is robust even in the presence of correlated noise and varying wave propagation directions. Good agreement is found between source parameters determined using converted DAS waveforms and on-land seismometers for both P- and S-wave records. The demonstrated ability to resolve source parameters using P-waves on horizontal ocean-bottom fibers is key for the implementation of DAS based earthquake early
30 warning, which will significantly improve hazard mitigation capabilities for offshore and tsunami earthquakes.

1 Introduction

In recent years, the implementation of distributed acoustic sensing (DAS) for seismological purposes is rapidly expanding, for both on land (e.g., Zhan, 2020; Fang et al., 2020; Jousset et al., 2018; Yu et al., 2019; Ajo-Franklin et al., 2019; Walter et al., 2020) and ocean-bottom (e.g., Sladen et al., 2019; Lior et al., 2021; Lindsey et al., 2019; Williams et al., 2019; Spica et al., 2020) applications. However, the use of DAS for several fundamental seismological tasks is yet to be fully established. These include earthquake location and source parameter (magnitude and stress drop) determination, both essential for harnessing DAS for earthquake early warning (EEW). But while application of source location have been investigated by recent studies (e.g., van den Ende and Ampuero, 2020; Lellouch et al., 2020; Lindsey et al., 2017), the ability to infer source parameters has not been investigated in detail (e.g., Lellouch et al., 2020).

One of the major hindrances for source parameter determination using DAS stems from the measurement type: DAS produces strain or strain-rate recordings while source models (e.g., Brune, 1970, Madariaga 1976; Sato and Hirasawa, 1973) rely on ground motions, i.e. displacements, velocities or accelerations. Thus, the ability to invert for the source properties using conventional methods depends on the ability to reliably convert strain (rate) measurements to ground motions. The conversion between strain (rate) to ground motion has been demonstrated by various previous studies (e.g. Daley et al., 2016; Lindsey et al., 2020; Paitz et al., 2020; Wang et al., 2018; Lior et al., 2020; van den Ende and Ampuero 2020). This conversion can be accurately done by spatial integration if one seismometer is co-located with the fiber, along straight portions that have uniform coupling (van den Ende and Ampuero 2020; Wang et al., 2018). When these conditions are unavailable, the common conversion approach consists of estimating the apparent phase velocities along the fiber and converting strain (rate) to ground velocity (acceleration) in the time- (e.g., Wang et al., 2018) or frequency- (e.g., Lindsey et al., 2020) domains, using the basic relation:

$$A = \dot{\epsilon}/p, \tag{1a}$$

$$V = \epsilon/p, \tag{1b}$$

where ϵ, $\dot{\epsilon}$, A, V and p are the strain, strain-rate, acceleration, velocity and apparent phase slowness along the fiber, respectively. These equations are valid for a single plane wave.

Since different seismic phases travel at different velocities, and frequently in different directions, the apparent velocity required to convert strain (rate) to ground motions may rapidly vary, and a single time-invariant value may bias the analysis. In addition, velocities may vary along a fiber due to local velocity structure and fiber orientation variations. The ability to robustly convert

DAS records to ground motions for signals containing varying phase velocities is key for harnessing DAS for early-warning and hazard mitigation purposes. Determining phase velocities via frequency-wavenumber (f-k) analysis (e.g., Lior et al., 2020; Lindsey et al., 2020; Paitz et al., 2020) can be challenging since sufficiently long cable segments and time-intervals are required to achieve adequate temporal and spatial frequency resolutions, in addition to delicate interpretation. To overcome this issue, a better suited approach to retrieve phase velocities as a function of time should be sought. In this study, we propose a method for continuous apparent phase velocity estimation using semblance-based local slant-stack transform (e.g., Neidell and Taner, 1971; Taner et al., 1979; Shi and Huo, 2019). This technique, commonly applied in exploration seismology (e.g., Tatham et al., 1983), is used here to estimate phase velocities as a function of time, facilitating a time-dependent conversion of DAS strain (rate) signals to ground motion records. We validate this conversion method using synthetic signals and apply it to ocean-bottom DAS earthquake records.

This manuscript is organized as follows. First, the slant stack algorithm is presented and validated using synthetic waveforms. Then, the approach is used to convert earthquakes recorded by ocean-bottom DAS to ground motions. Finally, source parameters are determined by fitting DAS observations with a source model, and compared with those determined using nearby seismometers. A comparison between the use of time-dependent, and constant apparent velocities is presented throughout the manuscript.

2 Slant stack transform for strain to ground motion conversion

Semblance-based local slant stack transform (e.g., Taner et al., 1979) is used to resolve apparent phase velocities as a function of time. This array-based technique measures the coherency (semblance) of plane waves recorded by several adjacent sensors. At each instance in time, a range of slowness values are tested. For each slowness, semblance is calculated by aligning the time-series recorded at different locations with respect to the middle station of a linear array (Shi and Huo, 2019):

$$sem(p_x, t) = \frac{1}{2L+1} \frac{\left[\sum_{j=-L}^{L} f\left(t+p_x(x_j-x_0)\right)\right]^2 + \left[\sum_{j=-L}^{L} h\left(t+p_x(x_j-x_0)\right)\right]^2}{\sum_{j=-L}^{L}\left[f\left(t+p_x(x_j-x_0)\right)^2 + h\left(t+p_x(x_j-x_0)\right)^2\right]}, \qquad (2)$$

where $f(t)$ and $h(t)$ are the real and imaginary parts of the seismic trace, $2L+1$ is the number of adjacent stations, and $x_j - x_0$ is the distance between station j and the middle station. The slowness with the highest semblance represents that of the most locally coherent plane wave at the specific time t. Including the Hilbert transform of the signal, $h(t)$, amounts to work with the

analytical signal, whose amplitude is the signal envelope, to allow for reliable semblance calculation at the zero-crossings of the original signal.

For optimal slowness determination, fiber segment lengths should correspond to the longest wavelength of interest. However, when implementing the local slant-stack transform, segment
95 lengths should be chosen to be upper bounded by the wavelength and the segment for which the signal remains coherent (coherency length), and lower bounded by the desired spatial and slowness resolutions (e.g., Ventosa et al., 2012). Spatial and slowness resolutions exhibit a trade-off since increasing the segment length will increase the slowness resolution and decrease the spatial resolution. Coherency lengths are expected to be small for DAS strain (rate) records since
100 they may be dominated by scattered waves (e.g., Lior et al., 2020), are extremely sensitive to local media heterogeneities (e.g., van den Ende and Ampuero, 2020; Singh et al., 2020) and fiber coupling (e.g., Sladen et al., 2019; Lior et al., 2020). Thus, in the current application, short cable segments are used, as further described.

The process of converting DAS strain (rate) signals to ground velocity (acceleration) is
105 detailed here, summarized in Fig. 1, and demonstrated using simulated data in the next section. Since seismic signals are a combination of various sources (e.g., earthquake waves, ambient noise, random signals), and may include dispersive waves, the signals need to be filtered at the frequency band of interest. The slant stack transform is applied per virtual seismometer along the fiber, using the $2L + 1$ adjacent traces (L on each side). The range of examined slowness values is
110 chosen to be between $\pm 0.01 \text{ s m}^{-1}$ with 0.2 s km^{-1} spacings, and at each time instance, the slowness value is determined based on the maximum semblance. The slowness time series (derived from semblance) may often be characterized by abrupt variations of value and sign (i.e., propagation direction). Thus, a moving average, with window size set to be equal to the signal's longest period of interest, is applied to the absolute value of the slowness. The sign is then
115 determined as the one that dominates each averaged window, i.e., the most recurrent sign. The filtered strain-rate signals are then converted to ground accelerations using Eq. (1). Slowness sign variations result in discontinuities in the converted strain-rate records, which are smoothed by additional filtering. The second filter may be chosen to be identical to the first, yet since it is applied to smooth discontinuities, different filters containing an upper frequency limit (i.e., low-
120 pass or band-pass), may be applied.
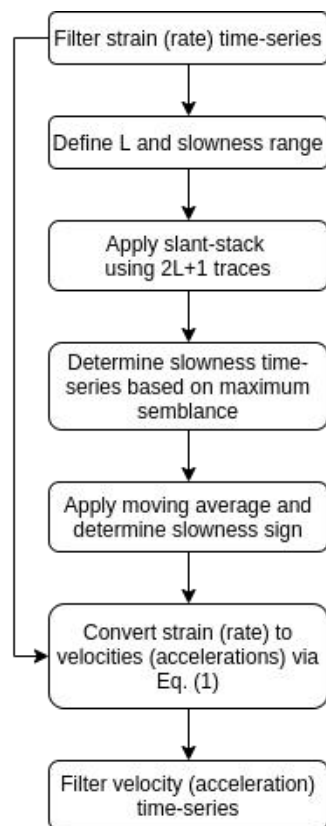
Figure 1: Flow chart detailing the conversion procedure from DAS strain (rate) signals to ground velocity (acceleration).

3 Validation using simulated earthquake records

3.1 Simulated data

To validate the proposed method, simulated earthquake waveforms are produced for a simple 2D velocity model representing an underwater sedimentary basin. A spectral-element based numerical simulation is done using the SPECFEM2D 7.0.0 code published under the CECILL V2 License (Komatitsch et al., 2012). The simple, though adequate, physical model is composed of two linear elastic sub-domains: a trapezoidal sedimentary layer with maximum depth of 100 m, characterized by P- and S-wave velocities of 1600 and 400 m s^{-1}, respectively, and density of 2000

125
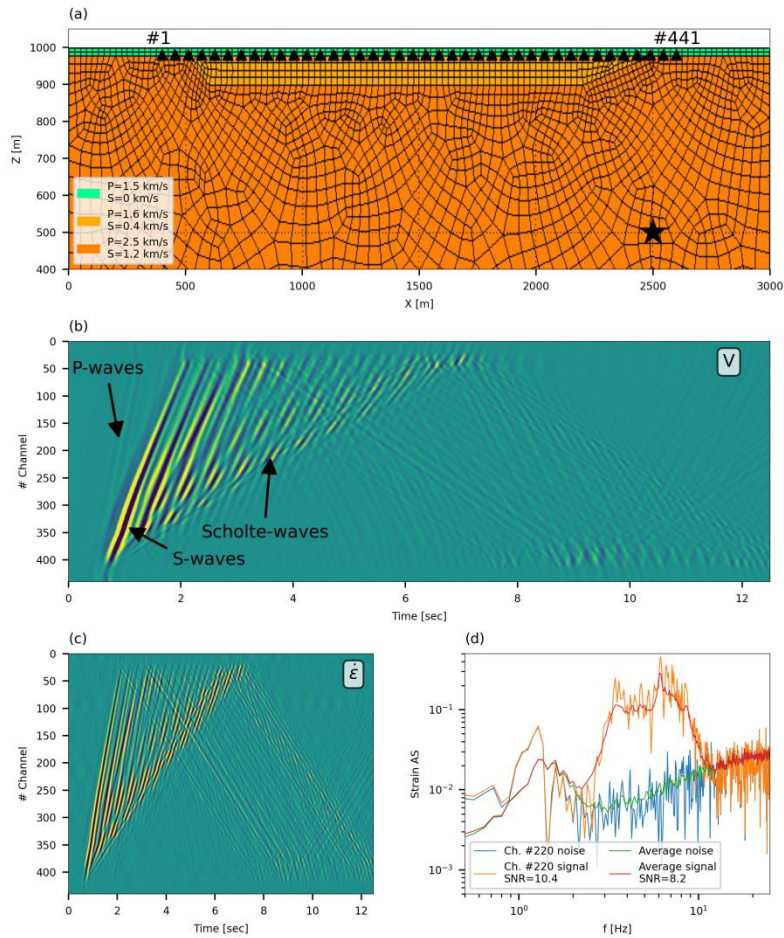
Figure 2: Velocity model and simulated velocity, strain-rate and noise data. Panel (a) shows the unstructured 2D numerical mesh: the double-couple source location is indicated by a black star and sensors are indicated by black triangles, equally spaced between X=400m to X=2600m (first and last sensor channel numbers are indicated). Panel (b) shows simulated velocity waveforms, with visible P-waves, S-waves and Scholte-waves. Panel (c) shows strain-rate signals added with ambient noise. Panel (d) shows simulated strain-rate and noise signals. Noise curves for channel #220 and averaged for all channels are indicated by blue and green curves, respectively. Signal added with noise for channel #220 and averaged for all channels are indicated by orange and red curves, respectively. SNR values are reported in the legend.

kg m^{-3} (yellow in Fig. 2a), overlying a bedrock with P- and S-wave velocities of 2500 and 1200 m s^{-1}, respectively, and density of 2200 kg m^{-3} (orange in Fig. 2a). These layers lie beneath a thin water

layer at 20 m depth with P- and S-wave velocities of 1500 and 0 m s⁻¹, respectively, and density of 1000 kg m⁻³ (green in Fig. 2a). The unstructured numerical mesh is generated using the Gmsh software (Geuzaine and Remacle, 2009) distributed under the terms of the GNU General Public License (GPL). It contains 2344 quadrilateral elements and, using an interpolation polynomial order

135   of 5, allows simulations up to 10 Hz maximum frequency. A double-couple point source is located at X = 2500 m, Z = 500 m and is time-modulated by a Ricker wavelet with a central frequency of 4 Hz, corresponding to a $M_w = 1$ earthquake. Receivers are regularly spaced at the bottom of the water layer from X = 400 m to X = 2600 m. Spatial and temporal sampling were set to be 5 m and 5 ms, respectively. These velocity waveforms represent 12.5 seconds of seismic recordings at 441

140   sensors, as seen in Fig. 2b. Since DAS can only record deformations along the optical fiber, simulated seismograms are single component, oriented along the array axis. These waves exhibit complex propagation patterns, with visible P- and S-waves, as well as surface waves reflected from the edges of the basin, providing an excellent test-case for the proposed algorithm.

   Simulated velocity waveforms were differentiated in time and space to obtain ground

145   accelerations and strain-rates, respectively, and the ability to convert the latter to the former via the proposed slant-stack approach is examined. Ambient noise measurements recorded on 22 July 2019 at a water depth of ~800 meters by an underwater cable deployed offshore Toulon, South of France (Sect. 4), were added to simulated strain-rates (Fig. 2c). These noise records, composed of secondary microseisms and instrumental noise, were differentiated to strain-rate and rescaled to

150   simulate challenging noise conditions, with an average signal-to-noise ratio (SNR) of 8.2 (Fig. 2d). Here, SNR was calculated as the root-mean-squares (RMS) ratio of average signal and noise amplitude spectra between 2 and 12 Hz. In-spite of the added noise, accelerations converted from strain-rates are compared to simulated accelerations (derived from simulated velocities by finite-difference time-derivative). Noise was not added to the latter, constituting a stringent algorithm

155   validation.

3.2 Strain-rate to ground acceleration conversion

   For the simulated data, waveforms were lowpass filtered at 12 Hz and short array segments of 100 m (L=10) were used to calculate the semblance and to convert each strain-rate signal into an acceleration seismogram. These segments are 25% shorter than the longest wavelength

160   observed for P-waves and provide a sufficient compromise between slowness and spatial resolution, allowing for reliable strain (rate) to ground motion conversion, as further shown. An example of the slant-stack conversion, applied to trace #220 of the simulated waveforms (Fig. 2b), is shown in Fig.

3. Panel (a) shows 7 seconds of strain-rate signals composed of P-waves (0.6-1.2 seconds), S-waves (1.2-2.5 seconds) and surface waves (2.5-7 seconds), including reflected waves with opposite

165   propagation direction (4.5-7 seconds). The semblance analysis in panel (b) shows phase slowness, corresponding to the maximum semblance, and smoothed slowness in orange circles and white curve, respectively. Red dots correspond to the ratio between strain-rates and accelerations (both differentiated from the simulated velocity waveforms) plotted at acceleration maxima and minima,
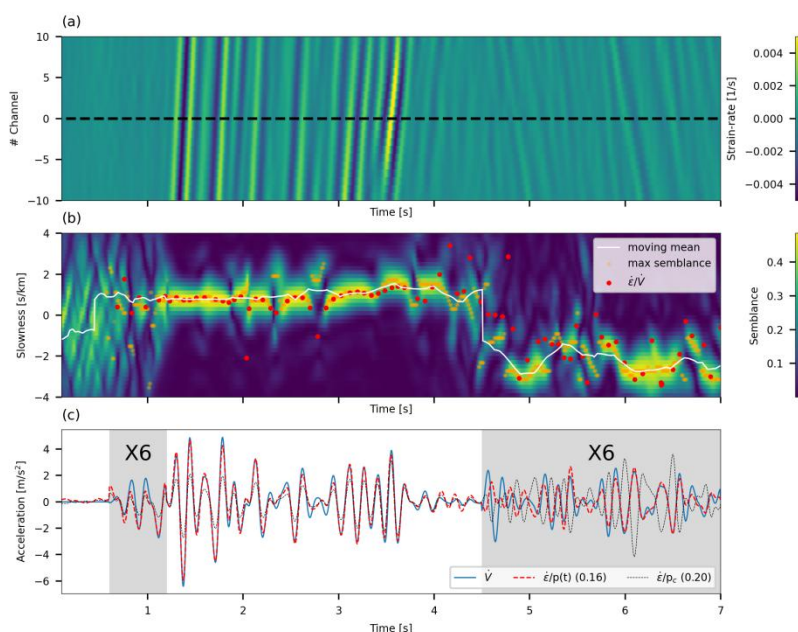
Figure 3: Slant-stack conversion for channel #220 of the simulated data. Top: strain-rate time series for 21 adjacent traces centered around channel #220 (dashed black line). Middle: Slowness as a function of time color coded by semblance values for channel #220. Slowness corresponding to the maximum semblance, and smoothed slowness are plotted in orange circles and a white curve, respectively. Red dots correspond to the ratio between strain-rates and accelerations, both differentiated from the simulated velocity waveforms. Bottom: accelerations, time-differentiated from simulated velocities (blue curve), compared with accelerations, space-differentiated from simulated velocities and converted using time-dependent slowness (red curve) and constant slowness (black curve). Standard deviations of the residuals between converted strain-rates (red and black curves) and time-differentiated velocities (blue curve) are indicated in the panel legend. Signals in regions marked in gray are amplified time 6 for easy comparison of low amplitude signals.

i.e., the optimal slowness values for strain-rate conversion. The similarity between the smoothed
170   slowness (white curve) and optimal slowness for conversion (red dots) suggests that the resolved
slowness may be reliably used for strain-rate to acceleration conversion. As expected, semblance
analysis resolves different velocities for different phases: average apparent phase velocities of 2.1,
1.3 and 0.6 km s^{-1} for P-waves, S-waves and surface waves, respectively (using the previously
indicated intervals). The bottom panel compares the acceleration signal (blue curve, differentiated
175   from simulated velocity) with strain rate converted accelerations using time-dependent slowness
(red curve) and a constant slowness of 1.4 s km^{-1}, averaged for the full 12.5 seconds simulation
(black curve).

Excellent agreement is observed between acceleration (blue curve in Fig. 3c) and converted
strain-rate, when the latter is obtained using time-dependent slowness (red curve in Fig. 3c). This
180   agreement persists for both fast (P-waves) and slow (S-waves and surface waves) phases,
demonstrating the ability to reliably resolve phase velocities even for short duration waves and
wavelengths longer than the fiber segments used for slant-stack analysis, e.g., P-waves . However,
when different waves interfere, the single plane wave assumption in Eq. (1) does not hold, the
phases of velocity and strain-rate signals may be misaligned (4.5-5.1 seconds) and phase velocities
185   may not be reliably resolved, resulting in lower quality conversion. When the intensity of such
effects fade, excellent agreement is again observed (5.1-7 seconds).

The use of a time-dependent slowness, rather than a constant value, is found to be
particularly advantageous when velocities abruptly vary and when propagation direction changes.
This is shown in Fig. 3c by comparing the constant slowness converted accelerations (black curve)
190   and time-dependent slowness converted accelerations (red curve) and is further illustrated in Fig. 4,
where strain-rate converted accelerations, using both time-dependent and constant slowness, are
compared with differentiated velocity for all simulated data. Comparing the residuals between
strain rate converted accelerations (panels c-d) and differentiated velocity (panel a) using time-
dependent slowness (panel e) and constant slowness (panel f) demonstrates the benefit of using
195   time-dependent slowness. The use of constant slowness produces larger residuals (panel f) than
the use of time-dependent slowness (panel e), especially for the direct P- and S-waves (0-3 seconds)
and for reflected waves (5-12.5 seconds). Standard deviations are thus systematically higher when
using constant slowness, as seen in panel b.

The conducted analysis, and excellent agreement between simulated strain rate converted
200   seismograms and acceleration signals, demonstrate the advantages of using the proposed slant-
stack based approach for strain-rate to ground motion conversion. Next, the technique is
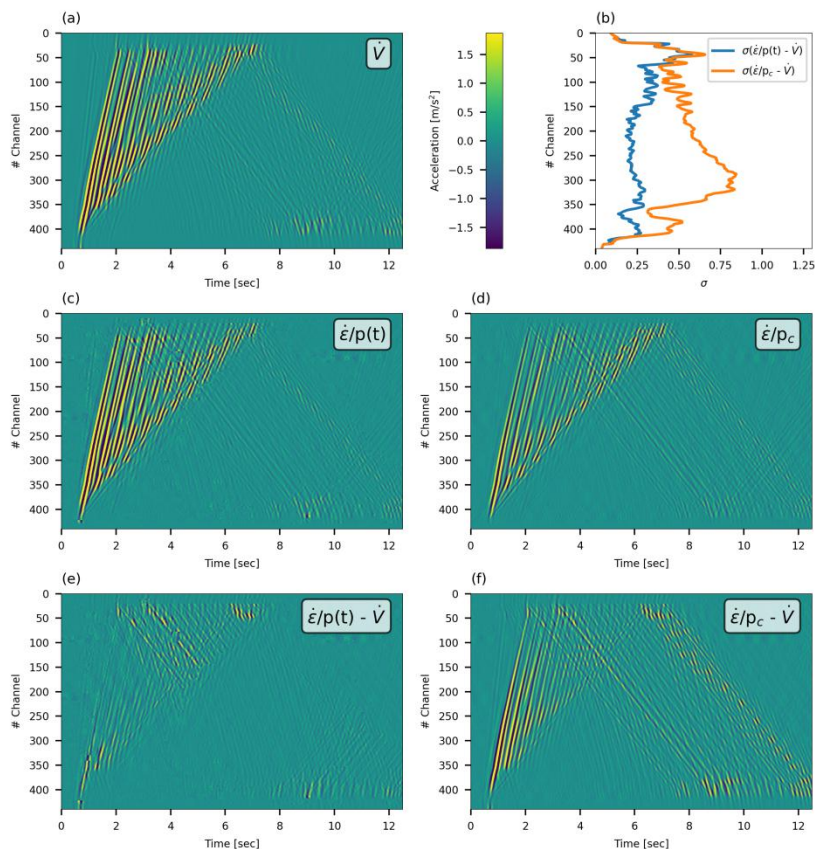
Figure 4: Comparison between simulated velocities time-differentiated to accelerations (panel a), and simulated velocities space-differentiated to strain-rate and converted to ground accelerations: using time-dependent slowness (panel c), and constant slowness (panel d). Panel (e) shows the residuals between accelerations in panels (c) and (a), and panel (f) shows the residuals between accelerations in panels (d) and (a). Standard deviations of the residuals for each recorded channel are plotted in panel (b) for the residuals in panel (e) (blue curve) and in panel (f) (orange curve).

implemented on earthquake recordings from three underwater DAS fibers in the Mediterranean, and the ability to determine their source parameters is demonstrated.

4 Data

205   For a real data application of the conversion technique, 8 local earthquakes are used. These were recorded by three dark ocean-bottom telecommunication cables deployed in the

Mediterranean Sea. This dataset is identical to the one used by Lior et al. (2020) and the cables' locations, bathymetric profiles and layout are detailed there. This information, as well as earthquake data, is briefly repeated here. Data was acquired by Géoazur on two cables deployed
210 offshore Methoni, south-west Greece, and one cable deployed offshore Toulon, South of France. In addition to DAS data, several on-land seismometers, installed near the cables, were available during the measurements. These will be later used (Sect. 6) to compare DAS and seismometer-derived source parameters. The earthquake data is detailed in Table 1 while magnitude and hypocentral distance distribution are shown in Fig. 5. In the latter, variations of hypocentral
215 distance correspond to the different analyzed fiber segments.

The two cables deployed offshore Greece are used for the HCMR (Hellenic Centre for Marine Research) and NESTOR (Neutrino Extended Submarine Telescope with Oceanographic Research) projects. The acquisitions were conducted on 18-19 and 19-25 April 2019 on the HCMR an NESTOR cables, respectively. A Febus A1 DAS interrogator was used, measuring strain-rate signals. Data
220 was sampled at 6 and 5 ms for HCMR and NESTOR, respectively, and gauge length and spatial sampling were both set to 19.2 m for both cables. These records amount to 688 and 1365 equally spaced channels for the 13.2 and 26.2 km long HCMR and NESTOR cables, respectively. In addition, 2 seismometers installed near the on-land end of the fibers were available during part of these campaigns, METN and METS.
225 The cable deployed offshore Toulon is used for the MEUST-NUMerEnv project (Mediterranean Eurocentre for Underwater Sciences and Technologies - Neutrino Mer Environnement) (Lamare, 2016) and was previously harnessed for DAS measurements by Sladen et

Table 1: Earthquakes used in this study.

Cable name	Origin time (UTC)	Magnitude (local)	Location (latitude, longitude, depth[km])	catalog
NESTOR	22/04/2019 19:26:06	3.3	37.4185, 20.6897, 11.0	Athens University
	23/04/2019 17:29:40	3.6	37.7753, 20.7658, 7.0	Athens University
	21/04/2019 22:11:47	2.0	36.8335, 22.0382, 2.0	Athens University
	23/04/2019 19:25:51	2.6	37.2528, 21.4593, 9.0	Athens University
HCMR	18/04/2019 21:44:42	3.7	37.57, 20.66, 8.0	EMSC
	19/04/2019 03:30:19	2.6	37.1523, 20.6662, 1.0	Athens University
MEUST	19/07/2019 21:16:57	2.6	44.374, 6.913, 2.6	Géoazur
	21/07/2019 23:01:58	2.4	42.516, 5.143, 2.0	Géoazur
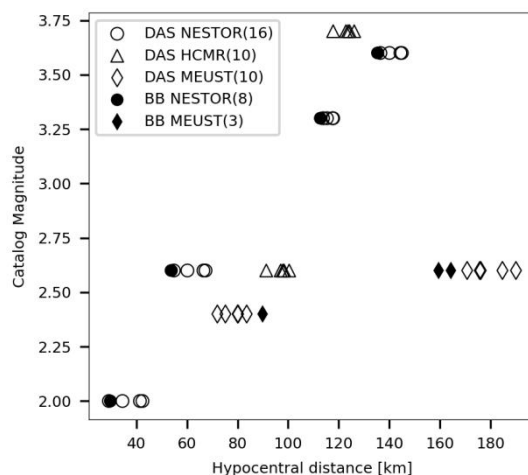
Figure 5: Earthquake catalog magnitude (M_L) as a function of hypocentral distances for the earthquakes in this study (Table 1). Hypocentral distances are measured to specific cable segments or broadband (BB) sensors. Solid and empty symbols correspond to seismometer and DAS data, respectively. Data for NESTOR, HCMR and MEUST are indicated by circles, triangles and diamonds, respectively, and the number of data points is indicated in parentheses in the legend.

al. (2019). The acquisitions were conducted on 11-31 July 2019 using a chirped-pulse hDAS interrogator developed by Aragon Photonics, measuring strain signals (Pastor-Graells et al., 2016; Fernandez-Ruiz et al., 2019; Williams et al., 2019). Data was sampled at 10 and 2 ms for the first and last 10 days of the campaign, respectively, and gauge length and spatial sampling were both set to 10 m. These records amount to 4480 equally spaced channels for the 44.8 km long cable. In addition, 2 seismometers were installed near the on-land end of the fiber, POSAN and POSAS.

5 Application to DAS recorded earthquakes

To demonstrate the performance of the proposed conversion approach, DAS strain (rate) earthquake signals are converted to ground velocities (accelerations). For each of the three cables, short fiber segments that exhibit coherent and continuous waveform recordings are chosen. Each section contains 29 traces, that are filtered using a 4-pole zero-phase Butterworth filter between 1 and 5 Hz. For different applications, a different filter may be used, as demonstrated in the next section. Filtered signals are converted to ground velocities or accelerations using fiber segments of ~380 m (L=10 for NESTOR and HCMR and L=19 for MEUST). Compared with simulated data, longer

segments are used in order to resolve faster seismic phases and longer wavelengths. Applying the conversion to DAS recorded earthquakes highlights body-wave arrivals, since these fast waves exhibit higher converted amplitudes compared with later arriving scattered waves and presignal
245 ambient noise. Figure 6 shows an example of strain conversion to ground velocities for an $M_L 2.6$ earthquake recorded by the MEUST cable at a hypocentral distance of 185 km, and Fig. 7 shows an example of strain-rate conversion to ground accelerations for an $M_L 3.6$ earthquake recorded by the NESTOR cable at a hypocentral distance of 140 km. In Fig. 6, mostly direct S-waves are shown, exhibiting unilateral wave propagation (panels a-c). The apparent velocity of the direct S-waves
250 (1.2-2.2 seconds) is determined to be ~2 km s^{-1} while later arriving waves travel at ~400 m s^{-1} (panel c), thus, as observed for the simulated data (Sect. 3), direct waves (panels b and d) exhibit
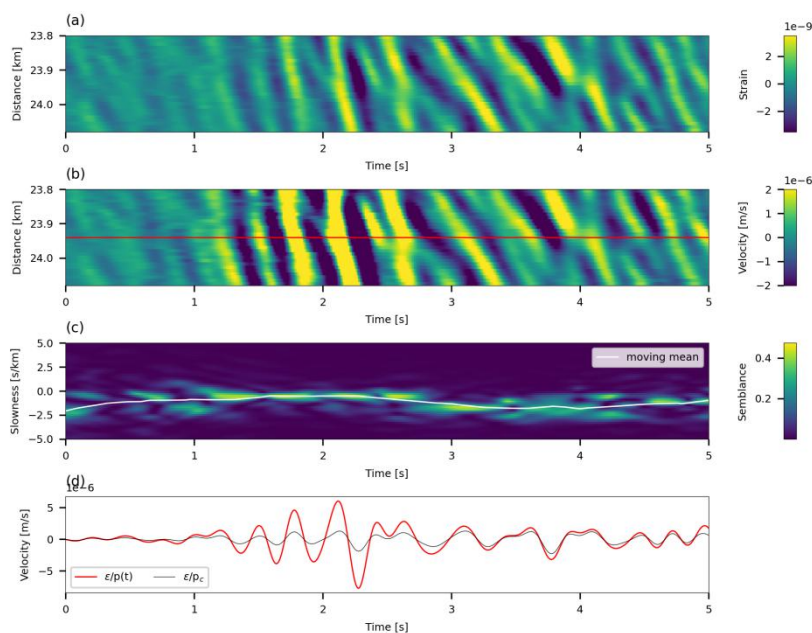
Figure 6: Slant-stack conversion for traces between 23.8 and 24.1 km along the MEUST cable of an M$_L$2.6 recorded at a hypocentral distance of 185km. 5 seconds around the direct S-wave arrival are shown. Panel (a): strain time series for 29 adjacent traces. Panel (b): Strain converted to velocities for all 29 traces. Panel (c): Slowness as a function of time color coded by semblance values for the middle channel, indicated by the red line in panel (b). White curve corresponds to smoothed slowness. Panel (d): Velocity converted using time-dependant slowness and constant slowness (corresponding to 404 m s^{-1}) are indicated by red and black curves, respectively.

higher converted velocity amplitudes compared to later phases. This is visualized by comparing the color-codes in panels (a) and (b), as well as strain converted velocities using time-dependent slowness (red curve) and constant slowness (black curve) in panel (d). Figure 7 shows both P- and S-waves, as well as presignal noise. In this example, scattered waves, and thus bilateral wave propagation, dominate the measurements (Lior et al., 2020), and several slowness sign flips are evident. The apparent velocity of first arriving S-waves (24-25 seconds) is 1.3 km s^{-1} while the average apparent velocity is 750 m s^{-1}, resulting in higher converted acceleration amplitudes for the direct waves. Ocean-bottom presignal noise is dominated by instrument related effects (e.g., Lior et al., 2020; Costa et al., 2019) and ambient noise. These signals are characterized by low apparent velocities, which results in low acceleration amplitudes, and facilitates easy identification
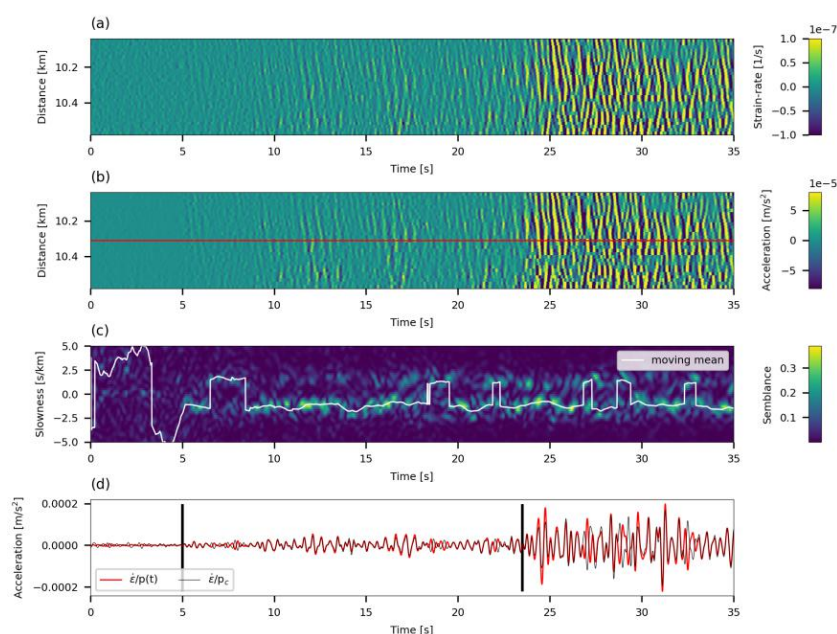
Figure 7: Slant-stack conversion for traces between 10.05 and 10.6 km along the NESTOR cable of an M$_L$3.6 recorded at a hypocentral distance of 140km. Both P- (~5 seconds) and S-wave (~23.5 seconds) arrival are shown. Panel (a): strain-rate time series for 29 adjacent traces. Panel (b): Strain-rate converted to accelerations for all 29 traces. Panel (c): Slowness as a function of time color coded by semblance values for the middle channel, indicated by the red line in panel (b). White curve corresponds to smoothed slowness. Panel (d): Velocity converted using time-dependent slowness and constant slowness (corresponding to 750 m s^{-1}) are indicated by red and black curves, respectively.

of the initial P-waves, subject to SNR conditions.

Next, the ability to invert for the source parameters, i.e., seismic moment, corner frequency and stress drop, is examined by converting strain (rate) records for predefined P- and S-wave intervals and fitting their spectra with an earthquake source model.

6 Implications for source parameter inversion

Seismic moment, source corner frequency, and stress drop are determined by fitting converted earthquake DAS signals with an earthquake source model. The source model chosen is the commonly used omega squared model (e.g., Brune, 1970, Madariaga 1976; Sato and Hirasawa, 1973) which describes the far-field body wave radiation for ground displacements, velocities and accelerations. The model is fit to the data via the single-step inversion of Lior and Ziv (2018). This approach is advantageous as model fitting is done in the time-domain, circumventing the time- to frequency-domain transformation and avoiding many spectral model fitting intricacies.

6.1 Source model

For ground displacements, velocities and accelerations, the omega-squared model subject to high frequency attenuation (Anderson and Hough, 1984) is given by:

$$\Omega(f) = \frac{\Omega_0}{1+(f/f_0)^2} exp(-\pi\kappa f), \tag{3a}$$

$$\dot{\Omega}(f) = 2\pi f \frac{\Omega_0}{1+(f/f_0)^2} exp(-\pi\kappa f), \tag{3b}$$

and

$$\ddot{\Omega}(f) = (2\pi f)^2 \frac{\Omega_0}{1+(f/f_0)^2} exp(-\pi\kappa f), \tag{3c}$$

respectively, where Ω_0 is the low-frequency displacement spectrum plateau, f is frequency, f_0 is the source corner frequency and κ is the attenuation parameter. The latter can be expressed as an attenuation corner frequency as $f_\kappa = 1/(\pi\kappa)$ (Eq. 4 of Lior and Ziv, 2018). The spectral parameters Ω_0 and f_0 correspond to the seismic moment, M_0, and stress drop, $\Delta\tau$, as:

$$M_0 = \Omega_0 \frac{4\pi\rho C^3 R}{U_{\varphi\theta}F_s}, \tag{4a}$$

$$\Delta\tau = \frac{7}{16} M_0 \left(\frac{f_0}{kC_S}\right)^3, \tag{4b}$$

where ρ is the density at the source, C is the wave velocity at the source (C_P and C_S for P- and S-waves, respectively), R is the hypocentral distance, $U_{\varphi\theta}$ is the radiation pattern, F_s is the free-

285   surface effect, and k is a constant which depends on the wave type and rupture speed (Madariaga, 1976). Equation (4b) applies to a circular crack (Eshelby, 1957) expanding isotropically at constant rupture speed. Parameter tuning is set as follows: ρ=2600 kg m^{-3}, C_P=5333 m s^{-1}, C_S=3200 m s^{-1}, $U_{\varphi\theta}$ equals 0.52 and 0.63 for P- and S-waves, respectively (Aki and Richards, 1980), F_s=2, and k equals 0.32 and 0.21 for P- and S-waves, respectively, corresponding to a rupture speed of 0.9Cs.

290   Using $F_s = 1.7$ instead of $F_s = 2$, as is sometimes used for ocean-bottom applications (e.g., Webb, 1998), will reduce magnitudes estimates by ~0.047, a minute difference compared to magnitude uncertainties, as shown in the next subsection.

6.2 From strain (rate) to source parameters

The spectral parameters are determined via the single-step inversion of Lior and Ziv (2018),
295   which resolves Ω_0, f_0 and κ using the time-domain signals, circumventing the time- to frequency-domain transformation, required by most source parameter inversion methods. The approach is fully detailed in Lior and Ziv (2018) and briefly summarized in Appendix A.

DAS strain (rate) data is converted to ground velocity (acceleration) for manually chosen P- and S-wave windows and source parameters are resolved. The procedure of determining the
300   frequency band of interest, strain (rate) to ground motions conversion, and model fitting is demonstrated in Fig. 8 for the S-waves of an M_L3.6 earthquake, recorded between 20.95 and 21.5 km along the NESTOR cable, at a hypocentral distance of 145 km. First, for the 29 traces composing each cable segment, strain (rate) signal and noise amplitude spectra (AS) are calculated, resampled (following the procedure described in McNamara and Buland, 2004) and
305   stacked for signal and presignal time-windows of equal length (dashed black and solid gray curves in panel a, respectively). The analyzed presignal noise is that recorded 2 minutes before the signals. The bandwidth for which frequency-specific SNR (signal AS(f) / noise AS(f)) is larger than 2 is used for subsequent analysis (solid black curve in panel a). If less than 3 discrete frequencies have high SNR, the recording is disregarded. To fully preserve the frequency-band of interest, the
310   filter's lower and upper corner frequencies are slightly decreased and increased by factors of $10^{-0.2}$ and $10^{0.2}$, respectively. Strain (rate) signals are then filtered (panel b), converted to ground velocities (accelerations) (panel c), and differentiated and/or integrated to obtain ground displacements, velocities and accelerations. Following each differentiation/integration, the forementioned filter is applied. The signals' RMS are calculated in the time-domain and source

315 parameters are determined as detailed in Appendix A. An example of the single-step inversion's results is shown in Fig. 8d where the best fitting model is plotted using Eq. (3c) and compared with observed stacked acceleration spectra, and Fig. 8e shows the best fitting parameter combination (Ω_0 , f_0 and κ) indicated by a gray star, in $log(f_0) - log(f_\kappa)$ space. Color code in panel e corresponds to the best fitting Ω_0 (for each $log(f_0) - log(f_\kappa)$ combination) and the contours
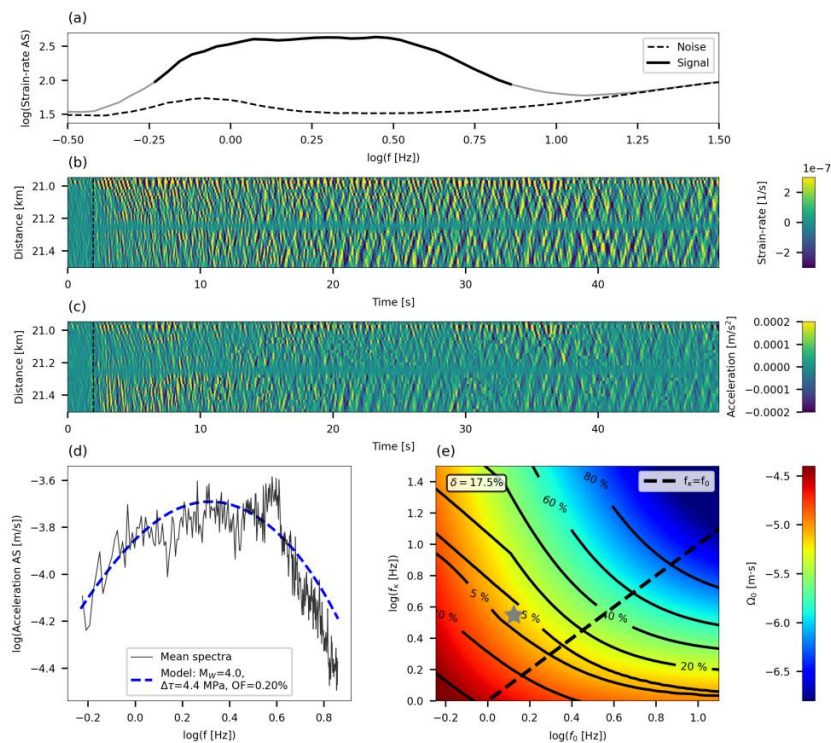
Figure 8: Source parameter inversion procedure for an M$_L$3.6 recorded at a hypocentral distance of 145km between 20.95 and 21.5 km along the NESTOR cable. Panel (a): stacked resampled signal and noise amplitude spectra (AS) are indicated by solid gray and dashed black curves, respectively. High-SNR signal (frequency specific SNR>2) is indicated by a solid black curve. Panel (b): strain-rate time series for 29 adjacent traces. Panel (c): Strain-rate converted to accelerations for all 29 traces. Panel (d): Stacked acceleration AS and best fitting earthquake model are plotted in black and blue curves, respectively. Panel (e): Contour diagram of the inversion's objective function in $log(f_0) - log(f_\kappa)$ space with color code corresponding to the best fitting Ω_0. The uncertainty parameter, δ, is indicated in the top-left corner, and the dashed black line indicates $f_0 = f_\kappa$.

320   correspond to the objective function's value. The solution exhibits a high degree of trade-off
between the values of f_0 and κ (panel e), yet good agreement is found between observed (black
curve) and modeled (blue curve) spectra (panel d).

        To further justify the use of time-dependent slowness, the presented source parameter
inversion was repeated using constant slowness for strain to ground motion conversion, and
325   goodness of fit parameters were compared. Slowness was set to be equal to the average absolute
slowness calculated for each seismogram and data interval. Here, the inversions' objective
functions (OF) are compared. The OF is a percentile measure of the discrepancy between modeled
and observed ground motion RMS (Eq. A2). Figure 9 plots the difference between OF for the time-
dependent slowness and constant slowness approaches as a function of catalog magnitude. Fits
330   obtained for data converted using time-dependent slowness generally exhibit lower OF values
(positive values in Fig. 9), i.e. their spectral shape is more similar to that predicted by the omega-
squared model. Model fits for four different earthquake records at several fiber segments are
plotted in Fig. 10. These plots demonstrate that the use of time-dependent (blue curves) or
constant slowness (orange curves) may result in different spectral shapes and lead to slightly
335   different source parameter estimates. For the recorded earthquakes, the largest disparity is
observed at low frequencies, which may result in different magnitude estimates (e.g., panels b and
d).
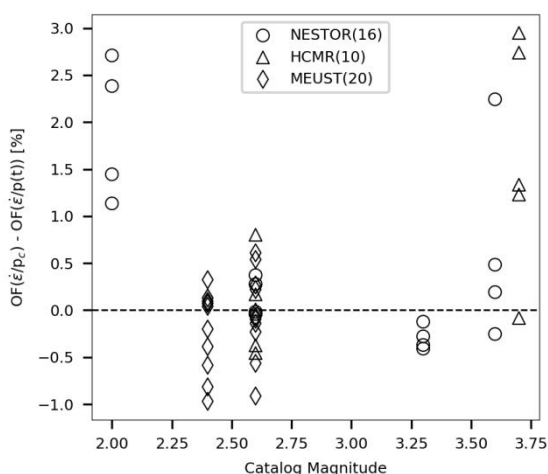
Figure 9: Model fit objective function (OF) differences between the constant slowness and
time-dependent slowness approaches, plotted as a function of catalog magnitude. Data for
NESTOR, HCMR and MEUST are indicated by circles, triangles and diamonds, respectively, and
the number of data points is indicated in parentheses in the legend.
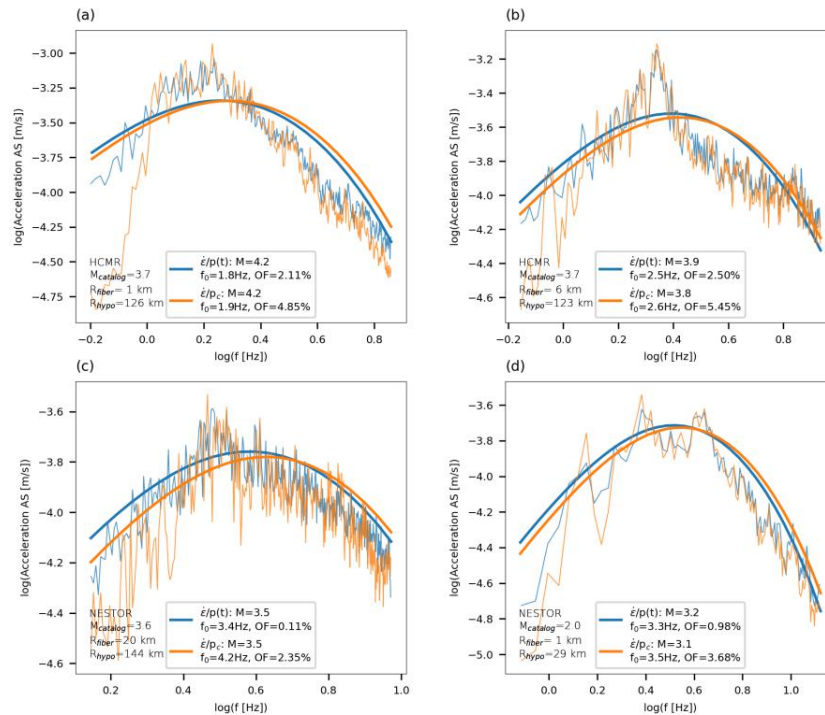
Figure 10: Model fits for four different earthquake records at several fiber segments. Stacked amplitude spectra and model fits corresponding to data converted using time-dependent slowness and constant slowness are indicated by blue and orange curves, respectively. Amplitude spectra are shown in thin curves while model fits are shown in thick curves. Resolved magnitudes, corner frequencies and the corresponding objective functions' values are reported in the panel legends. Cable name, catalog magnitudes ($M_{catalog}$), average distance along the fiber (R_{fiber}), and hypocentral distance (R_{hypo}) are reported on the bottom-left corner of each panel.

Moment magnitudes, stress drops and corner frequencies resolved using DAS data are found to be in good agreement with those estimated on adjacent on-land broadband seismometers. DAS P- and S-wave magnitude estimates are plotted as a function of average S-wave seismometer magnitudes in Fig. 11, and DAS S-wave f_0 and $\Delta\tau$ estimates are plotted as a function of average S-wave seismometer obtained parameters in Fig. 12. The low SNR conditions observed for P-waves, i.e. the narrow available frequency-band, did not allow for robust estimates of f_0 and $\Delta\tau$, which are thus not shown. A similar comparison with catalog magnitude is shown in Fig. 13, noting that local
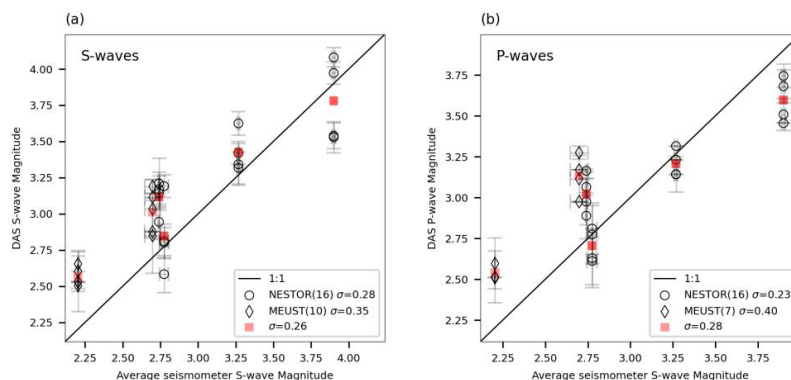
Figure 11: Comparison between DAS and seismometer magnitude estimates. Moment magnitudes estimated using DAS recorded S-waves (panel a) and P-waves (panel b) are plotted as a function of average magnitudes obtained using seismometer records. DAS event averaged magnitudes are plotted in red squares. The black curve is a 1:1 line. The number of data points and standard deviations to magnitude residuals are indicated in the legends. DAS magnitude errors are the standard deviations for magnitudes determined for each individual seismogram in the analyzed fiber segment, while seismometer errors are the standard deviations for single seismometer estimates.

345 and moment magnitudes may differ for small earthquakes (Deichmann, 2006). DAS parameter errors were calculated as the standard deviations of parameters determined for each individual seismogram in the analyzed fiber segment, while seismometer errors are the standard deviations of single seismometer estimates, when available. Data for the HCMR cable is not shown since seismometer gain was unavailable.

350 **7 Discussion**

      The proposed slant stack conversion approach relies on the ability to resolve the phase velocity of a single plane wave at every time instance. However, seismic records are often dominated by several waves, which may be dispersive (e.g. surface waves), characterized by different velocities, incidence angles, and exhibit complex propagation, scattering and interference

355 patterns. The analysis on simulated data in Sect. 3 demonstrates that when a single plane wave is considered, converted strain-rates are in excellent agreement with acceleration waveforms, while when two opposing plane waves interfere, the conversion's robustness is decreased (e.g., Fig. **3**). Careful filtering of DAS signals needs to be applied to isolate specific plane waves from DAS
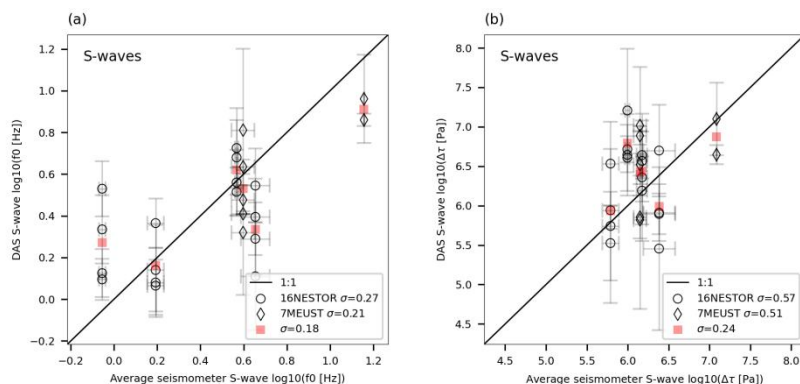
Figure 12: Comparison between DAS and seismometer source corner frequencies and stress drops. $log(f_0)$ (panel a) and $log(\Delta\tau)$ (panel b) estimated using DAS recorded S-waves are plotted as functions of average parameters obtained using seismometer records. DAS event averaged parameters are plotted in red squares. The black curve is a 1:1 line. The number of data points and standard deviations to parameter residuals are indicated in the legends. DAS parameter errors are the standard deviations for parameters determined for each individual seismogram in the analyzed fiber segment, while seismometer errors are the standard deviations for single seismometer estimates.

earthquake records, yet conversion errors may still result from inadequate slowness resolution,
360   incoherent plane waves, and noise. Full consideration of these issues is beyond the scope of this
manuscript. In-spite of these complexities, converted DAS signals allow for reliable magnitude
estimation, demonstrating the robustness of the conversion procedure.

Resolving source corner frequencies, and thus stress drops, for small and/or distant
earthquakes in unfavorable SNR conditions, is a challenging task since high frequency source
365   effects, i.e., f_0, are masked by high frequency attenuation, i.e., f_κ (e.g., Lior and Ziv, 2018). To
address this issue, Lior and Ziv (2018) introduced an uncertainty parameter, δ, a quality control
measure for the ambiguity between best fitting f_0 and κ. The value of δ is proportional to the area
enclosed within the 5% contour in $log(f_0) - log(f_\kappa)$ space (e.g., Fig. 8e). Lior and Ziv (2018) found
that solutions with high δ values (typically > 6%) usually exhibit a high degree of ambiguity
370   between f_0 and κ. For such cases, they implemented a two-step inversion approach, which
consists of determining a station, or in this case fiber segment, specific κ using low δ solutions and
repeating the inversion for Ω_0 and f_0. However, since for the data used in this study only few low δ
solutions were obtained, this technique is not implemented here. Thus, corner frequencies and
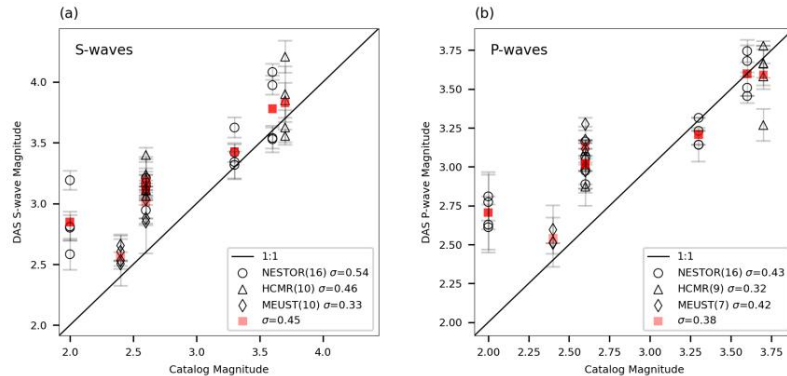
Figure 13: Comparison between DAS and catalog magnitude estimates. Moment magnitudes estimated using DAS recorded S-waves (panel a) and P-waves (panel b) are plotted as a function of catalog magnitudes. DAS event averaged magnitudes are plotted in red squares. The black curve is a 1:1 line. The number of data points and standard deviations to magnitude residuals are indicated in the legends. DAS magnitude errors are the standard deviations for magnitudes determined for each individual seismogram in the analyzed fiber segment.

stress drops are not well constrained. In-spite of the inability to reliably determine these
375   parameters, DAS and seismometer derived f_0 and $\Delta\tau$ are found to be in good agreement (Fig. 12).

Even in cases where f_0 and κ (and thus $\Delta\tau$) may not be well constrained, Ω_0, and thus
moment magnitudes, are reliably determined (Lior and Ziv, 2018). This is visualized in Fig. 8e,
where Ω_0 values (color code) are generally sub-parallel to the OF contours.

Magnitudes are reliably determined for both P- and S-waves (Fig. 11) in spite of the reduced
380   sensitivity of horizontal fibers to transverse deformations, as expected for P-waves. Recorded
deformation amplitudes are modulated by $cos^2\theta$, where θ is the wave's incidence angle with
respect to the fiber's axis (e.g., Ajo-Franklin et al., 2019; Kuvshinov, 2016; Mateeva et al., 2014;
Papp et al., 2017; Yu et al., 2018), thus, DAS measurements are mostly sensitive to deformations
along the fibers' axis, i.e. elongation and compression. Since direct P-waves are expected to arrive
385   at near vertical incidence angles, they would not induce significant deformations: while direct S-
wave arrivals are clearly identified for several fiber segments (e.g., Fig. 6), direct P-waves are not.
However, analyzed DAS records are dominated by low velocity waves, following both direct P- and
S-wave arrivals (e.g., Fig. 7). These are scattered P- and S-waves, propagating in a variety of
horizontal directions (Lior et al., 2020), which are easily measured on horizontal fibers, and used
390   here to infer source parameters. That earthquake magnitudes, determined by DAS measurements
of scattered waves, are in close agreement with both catalog magnitudes (Fig. 13) and

seismometer derived magnitudes (Fig. 11) indicates that these waves reliably represent the source characteristics and may be used for source parameter inversion.

The ability to infer source parameters using P-waves recorded on horizontal fibers is key for
395 harnessing DAS, specifically using underwater fibers, for EEW. The goal of EEW systems is to robustly and rapidly predict ground shaking intensities, an objective that is typically achieved by estimating earthquake source properties in real-time (e.g., Allen and Melger, 2019; Lior and Ziv, 2020). To this end, and in order to issue ground shaking alerts as early as possible, seismic observations should be obtained at close proximity to earthquake epicenters, and source
400 parameters should be estimated using both P- and S-waves. Since many of the most hazardous earthquakes on Earth occur underwater, the ability to determine source parameters using both P- and S-wave recorded by ocean-bottom DAS, will significantly improve the performance of EEW system for underwater earthquakes and enhance hazard mitigation capabilities.

8 Conclusions

405 In this study, the ability to convert DAS strain (rate) signals to ground motion records and resolve earthquake source parameters is demonstrated. An algorithm for DAS data to ground motion conversion is presented: apparent phase slowness is determined at every time instance using semblance based local slant-stack transform, and used to convert strain (rate) to ground velocities (accelerations). The algorithm is successful at resolving the apparent velocities of
410 different seismic phases. Validation using simulated waveforms reveals excellent agreement between simulated accelerations and converted strain-rate signals even in the presence of correlated noise and propagation direction variations. Application of the algorithm to 8 earthquakes recorded by ocean bottom DAS fibers in the Mediterranean Sea highlights fast waves (body-waves) since they exhibit high converted ground motion amplitudes compared with low-velocity scattered
415 waves and presignal ambient noise. Earthquake magnitudes and stress drops were determined for P- and S-waves using the single-step approach of Lior and Ziv (2018), circumventing the time- to frequency-domain transformation typically required for moment and corner frequency estimation. Close agreement is observed between source parameters determined using on-land broadband seismometers and ocean-bottom DAS, even when source corner frequencies and stress drops are
420 not well constrained due to significant high frequency attenuation. This ability to resolve earthquake magnitudes using P-waves recorded by horizontal ocean-bottom fibers is key for implementing DAS for EEW. The algorithm for strain (rate) conversion may be adapted for real-time applications and used in conjunction with real-time source parameter determination schemes (e.g.

Lior and Ziv, 2020) for a DAS-based EEW system. Harnessing DAS for EEW, specifically using
425 ocean-bottom fibers, will significantly improve hazard mitigation capabilities for underwater
earthquakes and tsunami earthquakes.

Appendix A

Lior and Ziv (2017, 2018) and Luco (1985) derived a set of ground motion RMS descriptions
based on Eq. 3 (Eq. 8 in Lior and Ziv, 2018):

$$D_{rms}^{model} = \Omega_0 \sqrt{\frac{\alpha_0}{\pi^{3/2}\kappa T}} \sqrt{G_{1,3}^{3,1}\left(\begin{matrix} \frac{1}{2} \\ 0, \frac{1}{2}, \frac{3}{2} \end{matrix} \middle| \alpha_0^2\right)}, \tag{A1b}$$

$$V_{rms}^{model} = 2\pi\Omega_0 \left(\frac{\alpha_0}{(2T)^{1/3}\pi\kappa}\right)^{3/2} \sqrt{\begin{matrix} 2Ci(2\alpha_0)[2\alpha_0 cos(2\alpha_0) + sin(2\alpha_0)] + \\ [\pi - 2Si(2\alpha_0)][cos(2\alpha_0) - 2\alpha_0 sin(2\alpha_0)] \end{matrix}}, \tag{A1b}$$

430 and

$$A_{rms}^{model} = (2\pi)^2 \Omega_0 \left(\frac{\alpha_0}{(2T)^{1/4}(\pi\kappa)^{5/4}}\right)^2 \sqrt{\begin{matrix} 2 - 2\alpha_0 Ci(2\alpha_0)[2\alpha_0 cos(2\alpha_0) + 3sin(2\alpha_0)] + \\ \alpha_0[\pi - 2Si(2\alpha_0)][2\alpha_0 sin(2\alpha_0) - 3cos(2\alpha_0)] \end{matrix}}, \tag{A1c}$$

where D_{rms}^{model}, V_{rms}^{model} and A_{rms}^{model} are displacements, velocities and accelerations RMS, respectively,
$G_{p,q}^{m,n}$, Ci and Si are the Meijer G, cosine integral and since integral functions, respectively, $\alpha_0 = \pi\kappa f_0$ and T is the used data interval, which is manually chosen in this application. Equations (A1)
435 constitute a set of 3 independent equations with 3 unknowns, for which the observations are
obtained in the time-domain (D_{rms}^{obs}, V_{rms}^{obs} and A_{rms}^{obs}) and the unknowns are the model's spectral
parameters (Ω_0, f_0 and κ). The objective function used is (Eq. 17 in Lior and Ziv, 2018):

$$OF = 100 \, max\left(\frac{|D_{rms}^{obs+} - D_{rms}^{model}|}{D_{rms}^{obs+}}, \frac{|V_{rms}^{obs} - V_{rms}^{model}|}{V_{rms}^{obs}}, \frac{|A_{rms}^{obs} - A_{rms}^{model}|}{A_{rms}^{obs}}\right), \tag{A2}$$

where D_{rms}^{obs+} is the corrected observed displacement RMS: since observed D_{rms}^{obs} is sensitive to low
frequencies, it is typically underestimated owing to the signals' limited frequency content.
440 Observed displacement RMS is corrected for the missing frequency content (Eq. 13 in Lior and Ziv,
2018): $D_{rms}^{obs+} = \sqrt{(D_{rms}^{obs})^2 + (D_{rms}^{corr})^2}$, where $D_{rms}^{corr} = \Omega_0\sqrt{f_I/T}$ (Eq. 15 in Lior and Ziv, 2018). In the
latter, f_I is the lowest resolvable frequency. This approach is implemented on both seismometer
recorded, and DAS recorded earthquakes. For seismometers, observed RMS are measured for the
vector length of the 3 components, while for DAS, seismogram specific RMS are calculated and

445 averaged for each fiber segment. The best fitting spectral parameters are obtained via grid-search algorithm for f_0 and κ, and Ω_0 is determined for each f_0 - κ combination by a random walk algorithm. Seismic moments and stress drops are then obtained using Eq. (4). When using Eq. (4a) for DAS recorded S-waves, Ω_0 is multiplied by $\sqrt{2}$ to compensate for the missing horizontal component.

450

Code and data availability: Simulated and observed DAS earthquakes are available on https://osf.io/98cnk/ and https://osf.io/4bjph/, respectively. Broadband seismometer data were acquired by Géoazur: data for the POSAN and POSAS stations were downloaded from RESIF
455 (http://seismology.resif.fr/, last accessed May 2020).

Author contributions: IL designed the presented algorithms, performed the analysis and wrote the initial draft; DM designed and performed the simulations; SS helped to adapt and implement the
460 slant-stack approach to DAS data. AS, JPA, DM, DR and SS contributed to the discussion, methodology, interpretation and presentation of the results.

Competing interests: The authors declare no competing interests.

465

Acknowledgments: This work and IL were supported by the SEAFOOD project, funded in part by grant ANR-17-CE04-0007 of the French Agence Nationale de la Recherche. Part of the project was also supported by Université Côte d'Azur IDEX program UCAJEDI ANR-15-IDEX-0001 and the
470 Doeblin Federation (FR2800 CNRS). We thank the team from the Centre de Physique des Particules de Marseille who facilitated the access to the MEUST infrastructure. The MEUST infrastructure is financed with the support of the CNRS/IN2P3, the Region Sud, France (CPER the State (DRRT), and the Europe (FEDER). We thank Stavroula Tsagkli, Katerina Tzamarioudaki and Christos Markou from NCSR Demokritos, the Greek Institute of Nuclear and Particle Physics, who maintain the
475 NESTOR cable infrastructure and facilitated the acquisition campaign. We thank Paris Pagonis from the Hellenic Centre for Marine Research who aided in the access to the HCMR cable. This

infrastructure is part of the European Multidisciplinary Seafloor and water column Observatory (EMSO).

References

480 Ajo-Franklin, J. B., Dou, S., Lindsey, N. J., Monga, I., Tracy, C., Robertson, M., Rodriguez Tribaldos, V., Ulrich, C., Freifeld, B., Daley, T. and Li, X.: Distributed Acoustic Sensing Using Dark Fiber for Near-Surface Characterization and Broadband Seismic Event Detection, Scientific Reports, 9(1), doi:10.1038/s41598-018-36675-8, 2019.

Anderson, J. G. and Hough, S. E.: A model for the shape of the fourier amplitude spectrum of acceleration at high frequencies, Bulletin of the Seismological Society of America, 74(5), 1969–1993, 1984.

485 Brune, J. N.: Tectonic stress and the spectra of seismic shear waves from earthquakes, Journal of Geophysical Research, 75(26), 4997–5009, doi:10.1029/JB075i026p04997, 1970.

Costa, L., Martins, H. F., Martin-Lopez, S., Fernandez-Ruiz, M. R. and Gonzalez-Herraez, M.: Fully Distributed Optical Fiber Strain Sensor With 10^{-12} ε/√Hz Sensitivity, Journal of Lightwave Technology, 37(18), 4487–4495, doi:10.1109/JLT.2019.2904560, 2019.

490 Daley, T. M., Miller, D. E., Dodds, K., Cook, P. and Freifeld, B. M.: Field testing of modular borehole monitoring with simultaneous distributed acoustic sensing and geophone vertical seismic profiles at Citronelle, Alabama: Field testing of MBM, Geophysical Prospecting, 64(5), 1318–1334, doi:10.1111/1365-2478.12324, 2016.

Deichmann, N.: Local Magnitude, a Moment Revisited, Bulletin of the Seismological Society of America, 96(4A), 1267–1277, doi:10.1785/0120050115, 2006.

495 Eshelby, J. D.: The determination of the elastic field of an ellipsoidal inclusion, and related problems, Proceedings of the Royal Society of London. Series A. Mathematical and Physical Sciences, 241(1226), 376–396, doi:10.1098/rspa.1957.0133, 1957.

Fang, G., Li, Y. E., Zhao, Y. and Martin, E. R.: Urban Near-Surface Seismic Monitoring Using Distributed Acoustic Sensing, Geophysical Research Letters, 47(6), doi:10.1029/2019GL086115, 2020.

500 Geuzaine, C. and Remacle, J.-F.: Gmsh: A 3-D finite element mesh generator with built-in pre- and post-processing facilities: THE GMSH PAPER, International Journal for Numerical Methods in Engineering, 79(11), 1309–1331, doi:10.1002/nme.2579, 2009.

Jousset, P., Reinsch, T., Ryberg, T., Blanck, H., Clarke, A., Aghayev, R., Hersir, G. P., Henninges, J., Weber, M. and Krawczyk, C. M.: Dynamic strain determination using fibre-optic cables allows imaging of seismological and

505   structural features, Nat Commun, 9(1), 2509, doi:10.1038/s41467-018-04860-y, 2018.

Keiiti, A. and Richards, P. G.: Quantitative seismology : theory and methods, W.H. Freeman, San Francisco., 1980.

Komatitsch, D., Vilotte, J.-P., Cristini, P., Labarta, J., Le Goff, N., Le Loher, P., Liu, Q., Martin, R., Matzen, R., Morency, C., Peter, D., Tape, C., Tromp, J., and Xie, Z.: SPECFEM2D v7.0.0 [software], Computational Infrastructure for Geodynamics, url: https://geodynamics.org/cig/software/specfem2d/, 2012.

510   Kuvshinov, B. N.: Interaction of helically wound fibre-optic cables with plane seismic waves: Interaction of fibre-optic cables, Geophysical Prospecting, 64(3), 671–688, doi:10.1111/1365-2478.12303, 2016.

Lamare, P.: The MEUST deep sea infrastructure in the Toulon site, edited by A. Capone, G. De Bonis, I. Di Palma, and C. Perrina, EPJ Web of Conferences, 116, 09001, doi:10.1051/epjconf/201611609001, 2016.

Lellouch, A., Yuan, S., Spica, Z., Biondi, B. and Ellsworth, W. L.: Seismic Velocity Estimation Using Passive

515   Downhole Distributed Acoustic Sensing Records: Examples From the San Andreas Fault Observatory at Depth, J. Geophys. Res. Solid Earth, 124(7), 6931–6948, doi:10.1029/2019JB017533, 2019.

Lellouch, A., Lindsey, N. J., Ellsworth, W. L. and Biondi, B. L.: Comparison between Distributed Acoustic Sensing and Geophones: Downhole Microseismic Monitoring of the FORGE Geothermal Experiment, Seismological Research Letters, 91(6), 3256–3268, doi:10.1785/0220200149, 2020.

520   Lindsey, N. J., Martin, E. R., Dreger, D. S., Freifeld, B., Cole, S., James, S. R., Biondi, B. L. and Ajo-Franklin, J. B.: Fiber-Optic Network Observations of Earthquake Wavefields: FIBER-OPTIC EARTHQUAKE OBSERVATIONS, Geophys. Res. Lett., 44(23), 11,792-11,799, doi:10.1002/2017GL075722, 2017.

Lindsey, N. J., Dawe, T. C. and Ajo-Franklin, J. B.: Illuminating seafloor faults and ocean dynamics with dark fiber distributed acoustic sensing, Science, 366(6469), 1103–1107, doi:10.1126/science.aay5881, 2019.

525   Lindsey, N. J., Rademacher, H. and Ajo-Franklin, J. B.: On the Broadband Instrument Response of Fiber-Optic DAS Arrays, J. Geophys. Res. Solid Earth, 125(2), doi:10.1029/2019JB018145, 2020.

Lior, I. and Ziv, A.: The Relation between Ground Acceleration and Earthquake Source Parameters: Theory and Observations, Bulletin of the Seismological Society of America, 107(2), 1012–1018, doi:10.1785/0120160251, 2017.

530 Lior, I. and Ziv, A.: The Relation Between Ground Motion, Earthquake Source Parameters, and Attenuation: Implications for Source Parameter Inversion and Ground Motion Prediction Equations, Journal of Geophysical Research: Solid Earth, 123(7), 5886–5901, doi:10.1029/2018JB015504, 2018.

Lior, I., Sladen, A., Rivet, D., Ampuero, J.-P., Hello, Y. M., Becerril, C., Martins, H. F., Lamare, P., Jestin, C., Tsagkli, S. and Markou, C.: On the Detection Capabilities of Underwater DAS, Earth and Space Science Open Archive, 535 doi:10.1002/essoar.10504330.1, 2020.

Luco, J. E.: On strong ground motion estimates based on models of the radiated spectrum, Bulletin of the Seismological Society of America, 75(3), 641–649, 1985.

Madariaga, R.: Dynamics of an expanding circular fault, Bulletin of the Seismological Society of America, 66(3), 639–666, 1976.

540 Mateeva, A., Lopez, J., Potters, H., Mestayer, J., Cox, B., Kiyashchenko, D., Wills, P., Grandi, S., Hornman, K., Kuvshinov, B., Berlang, W., Yang, Z. and Detomo, R.: Distributed acoustic sensing for reservoir monitoring with vertical seismic profiling: Distributed acoustic sensing (DAS) for reservoir monitoring with VSP, Geophysical Prospecting, 62(4), 679–692, doi:10.1111/1365-2478.12116, 2014.

McNamara, D. E. and Buland, R. P.: Ambient Noise Levels in the Continental United States, Bulletin of the 545 Seismological Society of America, 94(4), 1517–1527, doi:10.1785/012003001, 2004.

Neidell, N. S. and Taner, M. T.: Semblance and other Coherency Measures for Multichannel Data, Geophysics, 36(3), 482–497, doi:10.1190/1.1440186, 1971.

Paitz, P., Edme, P., Gräff, D., Walter, F., Doetsch, J., Chalari, A., Schmelzbach, C. and Fichtner, A.: Empirical Investigations of the Instrument Response for Distributed Acoustic Sensing (DAS) across 17 Octaves, Bulletin of 550 the Seismological Society of America, doi:10.1785/0120200185, 2020.

Papp, B., Donno, D., Martin, J. E. and Hartog, A. H.: A study of the geophysical response of distributed fibre optic acoustic sensors through laboratory-scale experiments: Geophysical response of fibre optic sensors, Geophysical Prospecting, 65(5), 1186–1204, doi:10.1111/1365-2478.12471, 2017.

Pastor-Graells, J., Martins, H. F., Garcia-Ruiz, A., Martin-Lopez, S. and Gonzalez-Herraez, M.: Single-shot 555 distributed temperature and strain tracking using direct detection phase-sensitive OTDR with chirped pulses, Optics Express, 24(12), 13121, doi:10.1364/OE.24.013121, 2016.

R. Fernández-Ruiz, M., Costa, L. and F. Martins, H.: Distributed Acoustic Sensing Using Chirped-Pulse Phase-Sensitive OTDR Technology, Sensors, 19(20), 4368, doi:10.3390/s19204368, 2019.

560   Sato, T. and Hirasawa, T.: Body wave spectra from propagating shear cracks., Journal of Physics of the Earth, 21(4), 415–431, doi:10.4294/jpe1952.21.415, 1973.

Shi, T. and Huo, S.: Complex Semblance and Its Application, Journal of Earth Science, 30(4), 849–852, doi:10.1007/s12583-018-0829-x, 2019.

Sladen, A., Rivet, D., Ampuero, J. P., De Barros, L., Hello, Y., Calbris, G. and Lamare, P.: Distributed sensing of earthquakes and ocean-solid Earth interactions on seafloor telecom cables, Nature Communications, 10(1), 1–8,

565   doi:10.1038/s41467-019-13793-z, 2019.

Taner, M. T., Koehler, F. and Sheriff, R. E.: Complex seismic trace analysis, GEOPHYSICS, 44(6), 1041–1063, doi:10.1190/1.1440994, 1979.

Tatham, R. H., Keeney, J. W. and Noponen, l.: Application of the tau-p transform (slant-stack) in processing seismic reflection data, Exploration Geophysics, 14(3–4), 163–172, doi:10.1071/EG983163, 1983.

570   van den Ende, M. P. A. and Ampuero, J.-P.: Evaluating Seismic Beamforming Capabilities of Distributed Acoustic Sensing Arrays, Solid Earth Discussions, doi:10.5194/se-2020-157, 2020.

Ventosa, S., Simon, C. and Schimmel, M.: Window length selection for optimum slowness resolution of the local-slant-stack transform, GEOPHYSICS, 77(2), V31–V40, doi:10.1190/geo2010-0326.1, 2012.

Walter, F., Gräff, D., Lindner, F., Paitz, P., Köpfli, M., Chmiel, M. and Fichtner, A.: Distributed acoustic sensing of

575   microseismic sources and wave propagation in glaciated terrain, Nature Communications, 11(1), doi:10.1038/s41467-020-15824-6, 2020.

Wang, H. F., Zeng, X., Miller, D. E., Fratta, D., Feigl, K. L., Thurber, C. H. and Mellors, R. J.: Ground motion response to an ML 4.3 earthquake using co-located distributed acoustic sensing and seismometer arrays, Geophysical Journal International, 213(3), 2020–2036, doi:10.1093/gji/ggy102, 2018.

580   Webb, S. C.: Broadband seismology and noise under the ocean, Reviews of Geophysics, 36(1), 105–142, doi:10.1029/97RG02287, 1998.

Williams, E. F., Fernández-Ruiz, M. R., Magalhaes, R., Vanthillo, R., Zhan, Z., González-Herráez, M. and Martins, H. F.: Distributed sensing of microseisms and teleseisms with submarine dark fibers, Nat Commun, 10(1), 5778, doi:10.1038/s41467-019-13262-7, 2019.

585 Yu, C., Zhan, Z., Lindsey, N. J., Ajo-Franklin, J. B. and Robertson, M.: The Potential of DAS in Teleseismic Studies: Insights From the Goldstone Experiment, Geophysical Research Letters, 46(3), 1320–1328, doi:10.1029/2018GL081195, 2019.

Zhan, Z.: Distributed Acoustic Sensing Turns Fiber-Optic Cables into Sensitive Seismic Antennas, Seismological Research Letters, 91(1), 1–15, doi:10.1785/0220190112, 2020.